J Mater Sci: Mater Electron (2017) 28:5222–5234
DOI 10.1007/s10854-016-6179-5

Synthesis and characterization of TiO_2–NiO and TiO_2–WO_3 nanocomposites

P. Pandi[1] · C. Gopinathan[1]

Received: 10 September 2016 / Accepted: 3 December 2016 / Published online: 1 February 2017

Abstract TiO_2–NiO and TiO_2–WO_3 nanocomposites were prepared by hydrothermal and surface modification methods. The samples were analyzed using X-ray diffraction, Scanning Electron Microscope images, Transmission Electron Microscope, Energy dispersive analysis, Zeta potential, Electrophoretic mobility and Photocatalysis activity measurement. XRD data sets of TiO_2–NiO, TiO_2–WO_3 powder nanocomposite have been studied for the inclusion of NiO, WO_3 on the anatase-rutile mixture phase of TiO_2 by Rietveld refinement. The cell parameters, phase fraction, the average grain size, strain and bond lengths between atoms of individual phases have been reported in the present work. Shifted positional co-ordinates of individual atoms in each phase have also been observed.

1 Introduction

In the emerging field of materials science and technology, significant evolution has been made using different transition metal oxide [1–3]. Among this, TiO_2 have solutions to the most pressing issues in energy generation with not detrimental to the environement. Therefore researchers are attracted towards the preparation of TiO_2 based solar cells and solar energy materials. Any modification in the semiconducting property or crystalline phase of the TiO_2 will change its application significantly thus making it an excellent candidate for wide applications in the field of energy and environment. From the previous prior research articles, the electrical conductivity of TiO_2 is poor under direct solar irradiation. By the incorporation of TiO_2 matrix with another semiconductor, the conductivity of TiO_2 was increased by reducing the photogenerated electron–hole pair recombination, properly directing the excess photogenerated electrons.

The performance photocatalytic activity is increases by the use of several mixtures of transition metal oxides such as TiO_2–V_2O_5 [4], TiO_2–SiO_2 [5], TiO_2–ZnO [6], TiO_2–SnO_2 [7, 8], TiO_2–CoO [9] and, TiO_2–SrO [10] that are nanocomposites. TiO_2, WO_3 and NiO are known as transition metal oxides with the direct band gap of 3.2–3.35 eV, 2.8 eV and 3.5–4.0 eV respectively. Recently, TiO_2–NiO [11] and TiO_2–WO_3 nanocomposites have been attracting more attention because of their better electrochromic behavior and outstanding performance as solid electrodes for solar cells [4]. The frontier of precision nanocomposites and comprehensive knowledge about structural parameters, structural factors relating properties and their relative performance in a certain application and also materials engineering leads to solving the new challenges.

In this research paper is mainly focused on the nanocomposites with the following objectives: Synthesis and Characterization of TiO_2 nanoparticles by hydrothermal method; TiO_2 nanoparticles were added to NiO and WO_3 respectively and nanocomposites were synthesized by surface modified process then annealed at 550 °C. The prepared samples were characterized by XRD and DRS UV-Vis-IR spectroscopy techniques. The particle size and

Electronic supplementary material The online version of this article (doi:10.1007/s10854-016-6179-5) contains supplementary material, which is available to authorized users.

✉ P. Pandi
pandipmc11@gmail.com

C. Gopinathan
cgnmku64@gmail.com

[1] Department of Solar Energy, School of Energy Sciences, Madurai Kamaraj University, Madurai 625021, Tamilnadu, India

morphology of the nanocomposites was studied by SEM and TEM technique respectively. Zeta Potential and Electrophoretic mobility is studied by Dynamic light scattering method. The elemental analysis was carried out by EDAX. In this research paper, for the first time, two mixed polymorphs of TiO_2 were investigated with the insertion of NiO and WO_3 by the Rietveld refinement process. Photocatalytic measurement was made under direct solar irradiation and eosin-Y used as dye for decomposition.

2 Synthesis of TiO_2 nanoparticles by hydrothermal method

The TiO_2 colloidal solution was prepared by hydrolysis of titanium tetra isopropoxide (TTIP) (Aldrich Chemicals, USA). In a typical process, 1 M of titanium tetra isopropoxide was mixed together with 4 M of acetic acid. The resultant solution was mixed with double distilled water and stirred vigorously for 1 h to obtain a clear solution. After an aging period of 24 h, the solution was kept in an oven at 70 °C for 12 h to the obtain $Ti(OH)_4$ colloidal solution. This was transferred into a stainless steel autoclave and placed in oven at 180 °C for 12 h. Then the autoclave was cooled down to room temperature. The solution was dried at 100 °C to get TiO_2 crystals and then crushed into fine powder with mortar and pestle [12–22].

2.1 Nanocomposite preparation

Nanocomposites were synthesized by dispersing 0.1 gm of Nickel oxide and 3 gm of TiO_2 in 50 ml of chloroform. This suspension was stirred for 3 h at 70 °C. After stirring, the mixture was filtered and repeatedly washed with chloroform and the resulting solid was dried in an oven at 100 °C for 1 h. This process was repeated for TiO_2–WO_3 nanocomposite preparation. Finally the fine powder was annealed at 550 °C for 1 h.

3 Result and discussion

3.1 Structural analysis

XRD pattern of both nanocomposites were recorded using Philips X'PERT PRO powder diffractometer with Cu–$K_{\alpha 1}$ ($\lambda = 1.54056$ Å) as the target in 2θ range of 3°–120° in steps of 0.05° as the intervals at SAIF Cochin. The TiO_2–NiO and TiO_2–WO_3 nanocomposites, the TiO_2 relative peak positions were consistent with the standard powder diffraction profile of anatase (JCPDS # 21-1272) and rutile (JCPDS # 21-1276), NiO (JCPDS # 47-1049), $NiTiO_3$ (JCPDS # 330960) and WO_3 (JCPDS # 43 1035) respectively. Figure 1 shows narrow peaks that were obtained by increasing both anatase and rutile diffracted crystallographic planes.

The nanocomposite structural features were analyzed using the Rietveld refinement method Jana 2006 software for the first time [23, 24]. In both the nanocomposites, TiO_2 crystallites exhibited two mixed polymorphs such tetragonal structure of anatase and rutile belongs to the space group of $I4_1/amd$ ($a = 3.785$ Å, $c = 9.514$ Å) and $P4_2/mnm$ ($a = 4.59373$ Å, $c = 2.95812$ Å) respectively. The input atomic coordinates for anatase was $x = y = z = 0$ for Ti and $x = y = 0$, $z = 0.2066$ for O. Similarly, that for rutile was $x = y = 0.30530$, $z = 0$ for O. The cubic crystal system of NiO belongs to the space group of $Fm\bar{3}m$ ($a = b = c = 4.17$ Å) and $x = y = z = 0$ Wyckoff position 4a for the Ni atom and also $x = y = z = 0.5$ for the 4b O atom [25]. The monoclinic crystal system of WO_3 belongs to the space group P_{21}/n ($a = 7.297$ Å, $b = 7.539$ Å, $c = 7.688$ Å) and WO_3 Wyckoff positions were taken from the reported results of Woodward et al. and Emil Indrea et al. [26, 27]. Figure 2 depicts the observed and calculated XRD profile for structural parameters, lattice parameters, peak shift, background profile and preferred orientations were used to minimize differences. The goodness of fit for all refinement process was close to unity.

The structural parameters and phase fractions of both the nanocomposites were obtained from the Rietveld refinements as shown in Table 1. The results of the reliable position refinement are presented in Table 2. Supplementary Figure 2a and Figure 2b give the observed and calculated structure factors of TiO_2–NiO and TiO_2–WO_3 nanocomposites with each phases. The anatase to rutile phase transformation occured with increase in annealing temperature and with respect to the oxygen vacancy. TiO_2 annealed at 550 °C showed better photocatalytic activity because it was 87.04% anatase and 12.96% rutile as per prior research papers [12, 28]. But in the obtained phase fraction of TiO_2–NiO nanocomposite, the phase fraction of the anatase decreased from 87.04 to 57.9%, when (O^{2-}) oxygen vacancy site in anatase TiO_2 was coupled with NiO. The $NiTiO_3$ diffraction peak was observed at $2\theta = 33.08°$, 35.65° from Figs. 1a and 2a and the annealed temperature of 550 °C was enough for the existence of $NiTiO_3$ [28].

In the case of TiO_2–WO_3 nanocomposite, it was noticed that the content of anatase decreased by 73.9% and was due to WO_3 incorporation on the surface of the tetragonal tunnel surrounded by TiO_6 octahedrons. Figure 2c shows the 3D electron density distributions of TiO_2 anatase and rutile are derived from the Rietveld analysis using visualization software called VESTA [29]. The Ti^{6+} ions octahedrally coordinated to six O^{2-} ions were distorted, with the apical (Ti–O)* bond length being slightly longer than the equatorial (Ti–O)# bond length. The Ti–Ti, W–O and Ni–O

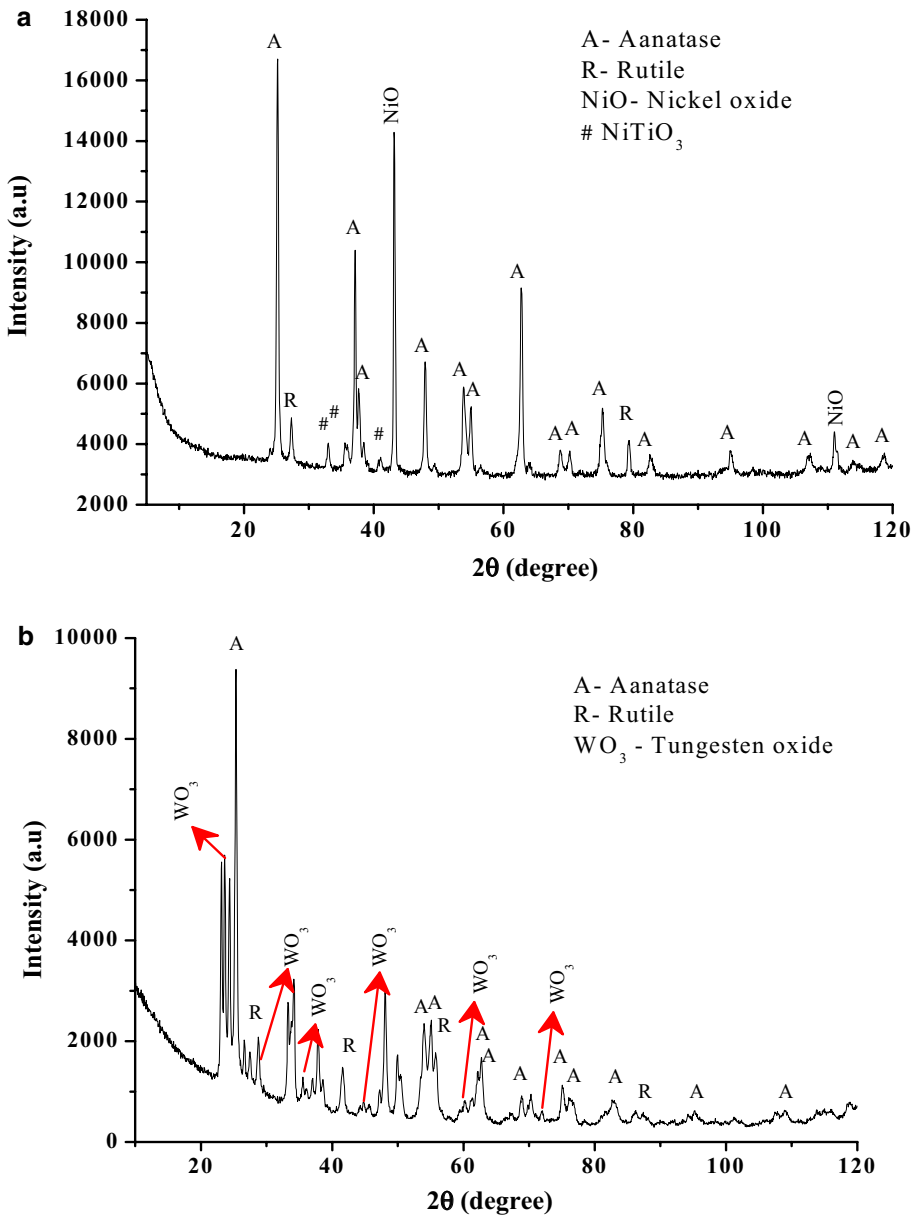

Fig. 1 XRD pattern of **a** TiO_2–NiO nanocomposite, **b** TiO_2–WO_3 nanocomposite

bond length is tabulated in Table 3. The rutile phase apical bond length (Ti–O#) and Ti–Ti bond lengths increased and another four equatorial oxygen atoms (Ti–O*) decreased respectively from the Cromer et al. [30] and Wolfgang Sigmund et al. [31] reported values, which could be due to lattice strain by adding NiO, WO_3 respectively. Moreover the inclusion of NiO, WO_3 to the TiO_2 matrix, produces little changes in the positions of both metal oxide systems due to energy minimization.

The size broadening due to the crystallite size distribution [32, 33] is given by

$$D = \frac{K\lambda}{B\cos\theta} \tag{1}$$

B is the FWHM (Full Width at Half Maximum) in radians. K is a constant—usually 0.9 for a spherical sample of cubic symmetry. λ is the wavelength used, d is the crystallite size (size of the coherently diffracting domain—different from particle size) and θ is the Bragg angle of the reflection. Strain broadens due to the strains present in the sample (due to lattice displacements of atoms from their original positions, surface strains, dislocations, impurities, non-stoichiometry in mixed systems, etc.—usually predominant in thin films, low order and nano structures).

$$B = 4e\tan\theta \tag{2}$$

B is the FWHM, e is the strain. The crystalline size was retarded by the insertion of NiO on both mixed

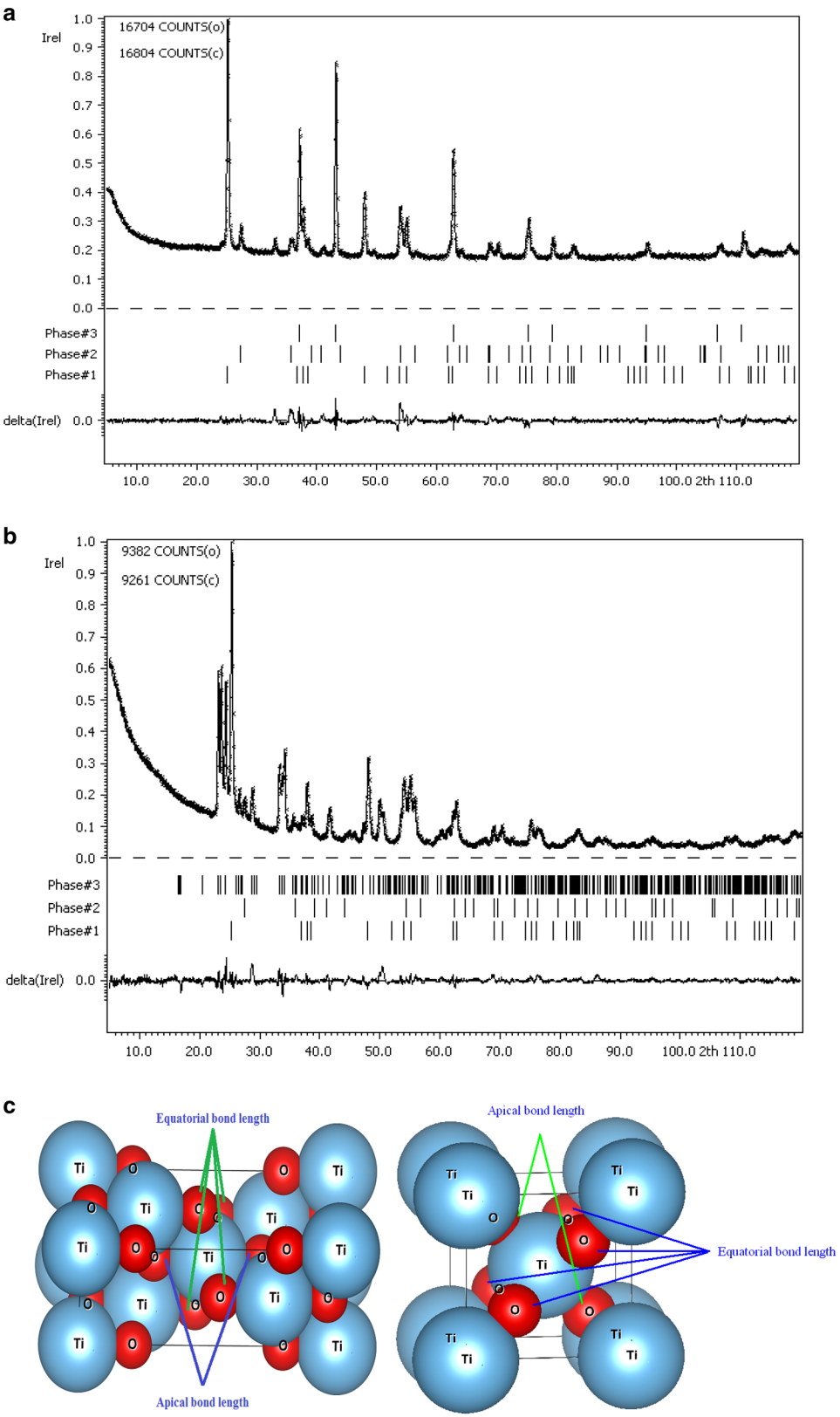

Fig. 2 **a** Refined X-ray powder profile for TiO_2–NiO nanocomposite (0 indicate $NiTiO_3$). **b** Refined X-ray powder profile for TiO_2–WO_3 nanocomposite. **c** 3D electron density and bond length of anatase and rutile TiO_2

Table 1 Structural parameters from the Rietveld refinement

Nanocomposite	TiO_2–NiO			TiO_2–WO_3		
Parameters	Phase #1	Phase #2	Phase #3	Phase #1	Phase #2	Phase #3
Phase #1						
a (Å)	3.7852	4.5968	4.1763	3.7833	4.5895	7.3128
b (Å)	3.7852	4.5968	4.1763	3.7833	4.5895	7.5221
c (Å)	9.5237	2.9961	4.1763	9.4929	2.9709	7.6944
Cell volume (Å)	136.5	63.3	72.8	135.9	62.6	423.3
R (obs)	1.02	0.18	1.55	2.57	2.56	2.43
wR (obs)	1.46	0.37	2.52	3.11	2.96	3.06
Phase fraction %	57.9	15.4	26.7	73.9	9.4	16.7
D (nm)[a]	23.24	15.33	44.92	30.96	25.49	19.57
Strain $\times 10^{-2}$ [a]	0.11	0.10	0.13	0.154	0.153	−0.03

[a]Using Scherer's formula

Table 2 Bond length for TiO_2–NiO nanocomposite

Nanocomposite	Atoms	TiO_2–NiO			TiO_2–WO_3		
Positions		x	y	z	x	y	z
Phase #1	Ti	0	0	0	0	0	0
	O	0	0	0.2507	0	0	0.207
Phase #2	Ti	0	0	0	0	0	0
	O	0.2931	0.2931	0	0.3124	0.3124	0
Phase #3	Ni	0	0	0			
	O	0.5	0.5	0.5			
	W1				0.2407	0.0243	0.2591
	W2				0.2479	0.0279	0.7425
	O1				0.0211	0.0732	0.2391
	O2				1.0364	0.4331	0.2953
	O3				0.2821	0.2602	0.287
	O4				0.235	0.2145	0.7919
	O5				0.3033	0.0021	0.0212
	O6				0.3001	0.5485	1.1663

Table 3 Bond length for nanocomposite

Nanocomposite	Bond		Ti–O (*)	Ti–O (#)	Ti–Ti	Ni–O	W_1–O_4	W_1–O_6	W_2–O_2	W_2–O_3	W_2–O_5	W_2–O_7
TiO_2–NiO	TiO_2	A	1.9388	1.9600	3.0415							
		R	1.9055	2.0132	2.9961							
	NiO					2.0882						
TiO_2–WO_3	TiO_2	A	1.9353	1.9647	3.0349							
		R	1.9207	2.0276	2.9709							
	WO_3						1.8132	1.8947	1.6336	1.7784	1.4573	0.7007

anatase-rutile phase TiO_2, so that anatase was 23.24 nm, rutile was 15.33 nm, which can be compared to previous research papers. The crystalline size of NiO was 44.92 nm. But in the case of TiO_2–WO_3 nanocomposite, the size of the crystallites increased. Anatase was 30.96 nm and rutile was 25.49 nm due to the accumulation of WO_3 on anatase-rutile mixture of TiO_2. The size of WO_3 crystallites was 19.57 nm (Table 1).

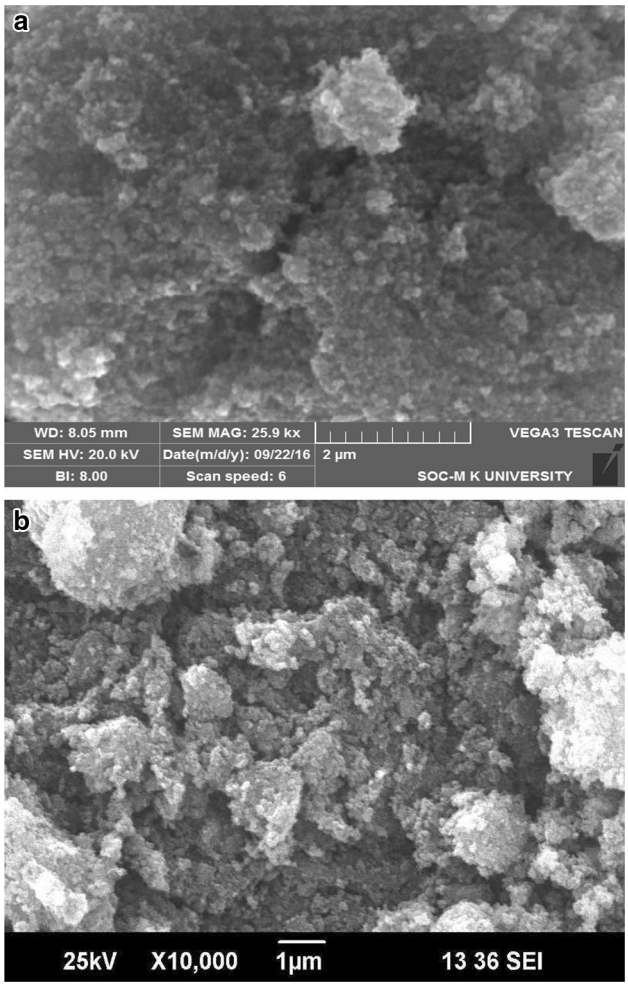

Fig. 3 **a** SEM image of TiO_2–NiO nanocomposites. **b** SEM image of TiO_2–WO_3 nanocomposites

3.2 Morphological analysis

The nanostructure of the TiO_2–NiO and TiO_2–WO_3 nanocomposites were observed by SEM as shown in Fig. 3. The morphologies of TiO_2–NiO and TiO_2–WO_3 nanocomposite could be seen as particles with great aggregation and the particle size was around few tens of nanometer. Figure 3 evidently illustrate that the close contact nanoparticles served as a beneficial path to easily move electrons from one grain to another. Figure 3 show that TiO_2–NiO and TiO_2–WO_3 nanocomposites receive an increasing attention in the field of solar materials and solar cell application due to their small grain size and high density of grain boundaries.

Figures 4 and 5 illustrate TiO_2–NiO and TiO_2–WO_3 nanocomposites the particle size distribution examined by the TEM. In TiO_2–NiO nanocomposites size of the particles was not uniform but had a spherical, cubic and hexagonal shape as shown in Fig. 4a, b. The size of the nanoparticles was in the range of 31–44 nm and the particle size distribution was completely crystallized. Figure 5a, a suggests that, on anatase-rutile mixed phase TiO_2, WO_3 nanoparticles tend to aggregate with each other to form bigger particle size distribution as compared to TiO_2–NiO nanocomposites. The TiO_2–WO_3 nanocomposite size distributions matured as large as 18–64 nm due to recrystallization.

Figure 4d, e illustrate the direct evidence of crystalline nature of NiO, anatase and rutile TiO_2 nanoparticles. HRTEM images shows clear lattice fringes, which allowed for the identification of crystallographic spacing. Figure 4d shows the interplanar distance of 0.352 nm was close to the d spacing of the (1 0 1) planes of the anatase TiO_2. Figure 4e shows the lattice spacing of 0.25 nm was related to the (1 0 1) plane of rutile TiO_2. Moreover the lattice spacing of 0.27 nm was correlated to the (1 0 4) plane of $NiTiO_3$ (JCPDS# 330960), which confirms the presence of anatase TiO_2, rutile TiO_2 and NiO. Figure 4f shows the Selected Area Electron Diffraction (SAED) pattern of TiO_2–NiO nanocomposite. The synthesized TiO_2–NiO nanocomposite was further confirmed by the result of SAED pattern. All reflected crystallographic plane in electron diffraction pattern of TiO_2–NiO composite were good agreement with the XRD results.

The interplanar distance of 0.38 nm, 0.352 nm and 0.25 nm was corresponds to (0 0 2) planes of the WO_3, (1 0 1) planes of the anatase TiO_2, (1 0 1) plane of rutile TiO_2 as shown in Fig. 5d, e, which confirms the presence of anatase TiO_2, rutile TiO_2 and WO_3. Figure 5f shows the SAED pattern of TiO_2–WO_3 nanocomposite were good agreement with the XRD results.

The chemical composition of the prepared TiO_2–NiO nanocomposites are presented in Fig. 6 and Table 4. The content of TiO_2–NiO nanocomposites of both anatase and rutile were high (at.%) as compared to NiO.

3.3 DRS UV-Vis-IR analysis

The optical absorbance spectrum of nanocomposite is shown in Fig. 7a, b, which showing strong absorption and this could be due to the surface morphology of both the nanocomposites. The different particle size of nanocomposites absorbed wavelengths in this range and it was blue and red shifted. In order to determine the optical band gap of the nanocomposites, the absorption coefficient (α) was calculated from the absorbance spectrums using Eq. (3).

$$(\alpha h\nu) = A(h\nu - E_g)^n \tag{3}$$

where E_g is the optical bandgap. Figure 7c, d gives the typical Tauc plot of $(\alpha h\nu)^2$ vs $h\nu$ for TiO_2–NiO and TiO_2–WO_3 nanocomposites. The values of band gap have been estimated by taking the intercept of the extrapolation to zero

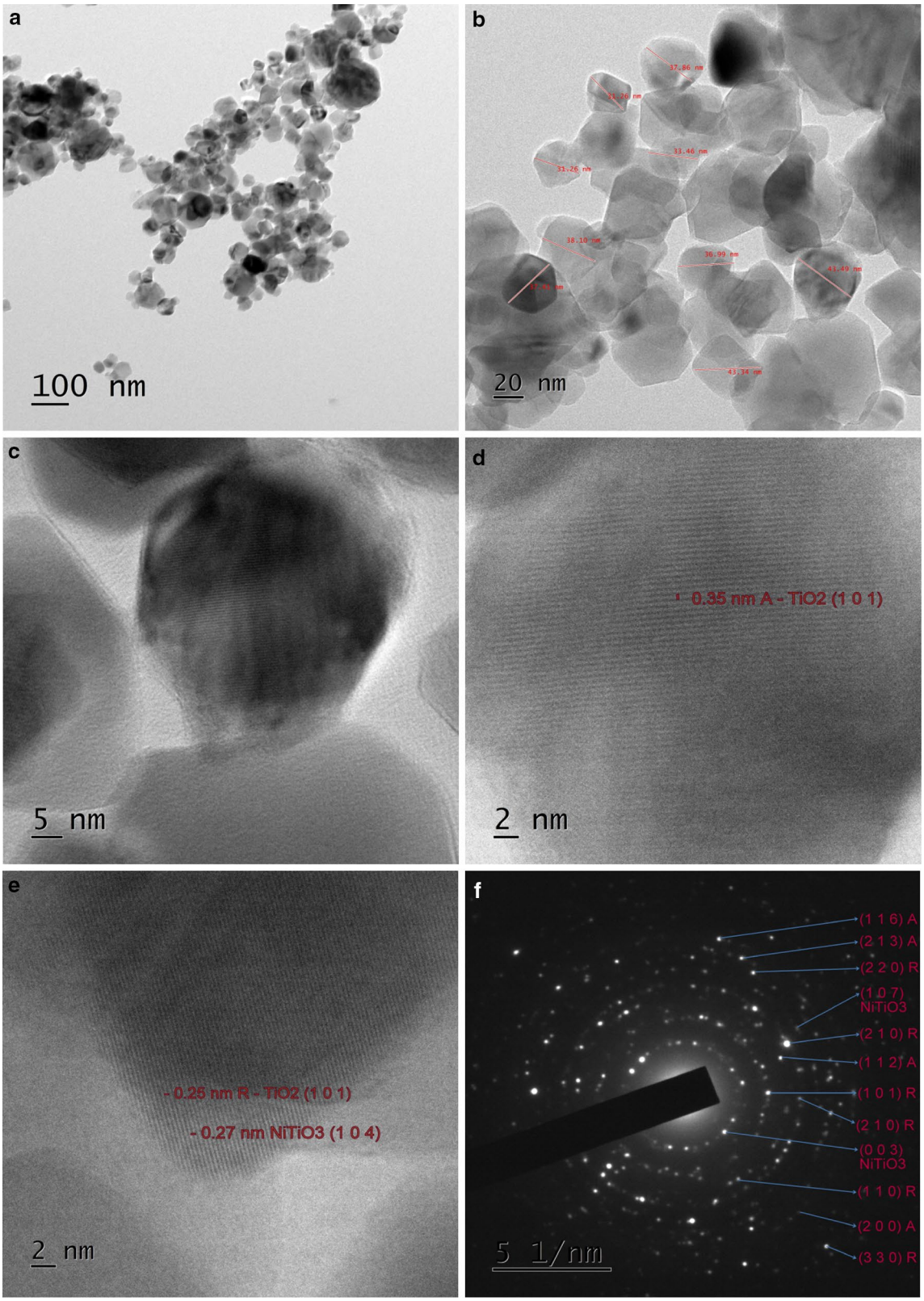

Fig. 4 **a–c** TEM images ofnanocompositesTiO$_2$–NiO, **d** HRTEM image of anatase TiO$_2$, **e** HRTEM image of rutile TiO$_2$ and NiTiO$_3$ and **f** SAED pattern of TiO$_2$–NiO nanocomposite

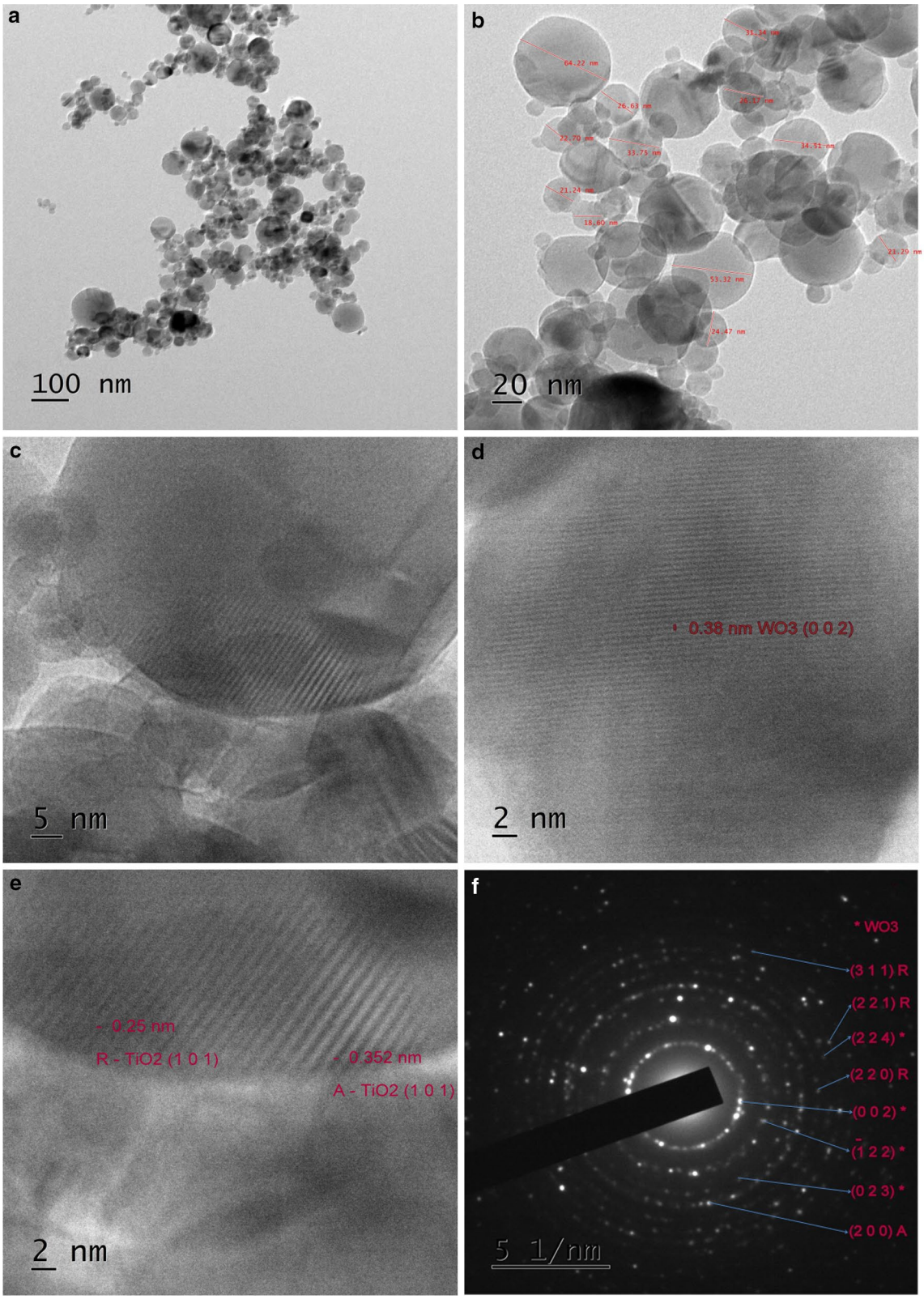

Fig. 5 **a**–**c** TEM images of nanocomposites TiO_2–WO_3, **d** HRTEM image of WO_3 and, **e** HRTEM image of rutile TiO_2 and anatase TiO_2 and **f** SAED pattern of TiO_2–WO_3 nanocomposite

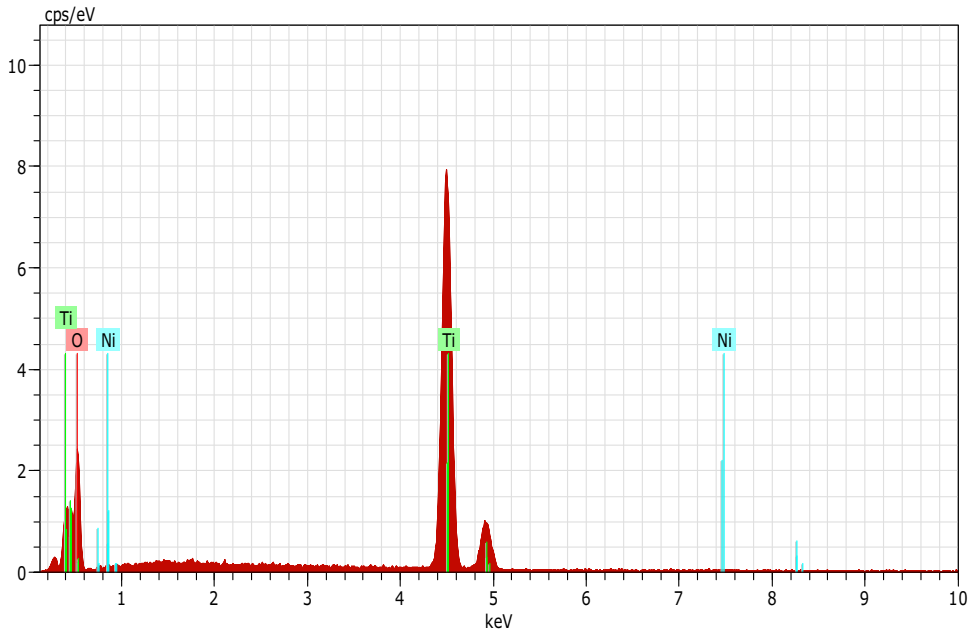

Fig. 6 Elemental analysis of TiO_2–NiO nanocomposites

Table 4 Elemental analysis of TiO_2–NiO nanocomposites

Elements	Atomic %	Weight %
O	50.27	75.17
Ti	49.56	24.76
Ni	0.18	0.07

absorption co-efficient with photon energy axis. Figure 7c, d indicates the direct allowed transition present in the TiO_2–NiO and TiO_2–WO_3 nanocomposites.

The band gap value of TiO_2–NiO nanocomposite decreased to 2.44 eV and this was due to the structural parameters. Ti –Ti bond length in anatase phase was greater than in rutile phase, whereas apical and equatorial bond lengths were shorter. The anatase to rutile phase fractions decreased when annealed at 550 °C after the inclusion of NiO to TiO_2 matrix. These structural changes led to different electronic configurations. Moreover NiO (6.67 g/cm^3) had higher density than rutile (4.23 g/cm^3) and anatase (3.78 g/cm^3) phase TiO_2, therefore the band gap values of TiO_2–NiO nanocomposite at 550 °C (2.44 eV) decreased. The tauc plot (Fig. 7d) of TiO_2–WO_3 nanocomposite annealed at 550 °C depicted band gap value of 2.40 eV. Because of the annealing temperature led to bigger particle size due to the agglomerated WO_3 particles on the TiO_2 matrix as shown in Fig. 5b. Tables 1 and 2 show the structural parameters for the 550 °C annealed TiO_2–NiO and TiO_2–WO_3 nanocomposites.

3.4 Photocatalytic analysis

The photocatalytic activity for anatase, rutile and two mixed polymorphisms of TiO_2 with NiO, WO_3 nanocomposite yielded good results due to the competing charge transportation to the surface and comparative declination in the surface area due to the large crystallites. In addition, after the insertion of NiO or WO_3 to the TiO_2 systems, changes could be observed in the unit cell, positions and bond lengths, which are key factors for their peculiar properties as compared to parent system. The energy minimization (equilibrium) of the TiO_2–NiO or TiO_2–WO_3 system led to internal rearrangements within the constrained, which could be resovled many problems such as oxygen defects, lattice defects at its surface and interface, electron–hole pair recombinations and so on.

The photocatalytic activity was assessed by degrading 0.1 mM of eosin-Y in aqueous solution (eosin-Y concentration 0.1mM; TiO_2–NiO/(or TiO_2–WO_3): 0.2 gm). The changes of eosin-Y concentration with direct solar irradiation were observed by measuring the absorption spectra using a Thermo-spectronic UV–Vis spectrometer. The samples were taken out every 10 min to record the absorption spectra. Figure 8a shows the intensity of the absorbance spectra of eosin-Y, with the presence of TiO_2–NiO nanocomposites, which decreased after direct solar irradiation was incident on it. In nanocomposites, absorption at 516 nm was taken into account to determine the rate of degradation. Figure 8c shows the absorbance spectra of direct solar irradiated eosin-Y solution which had better photocatalytic activity.

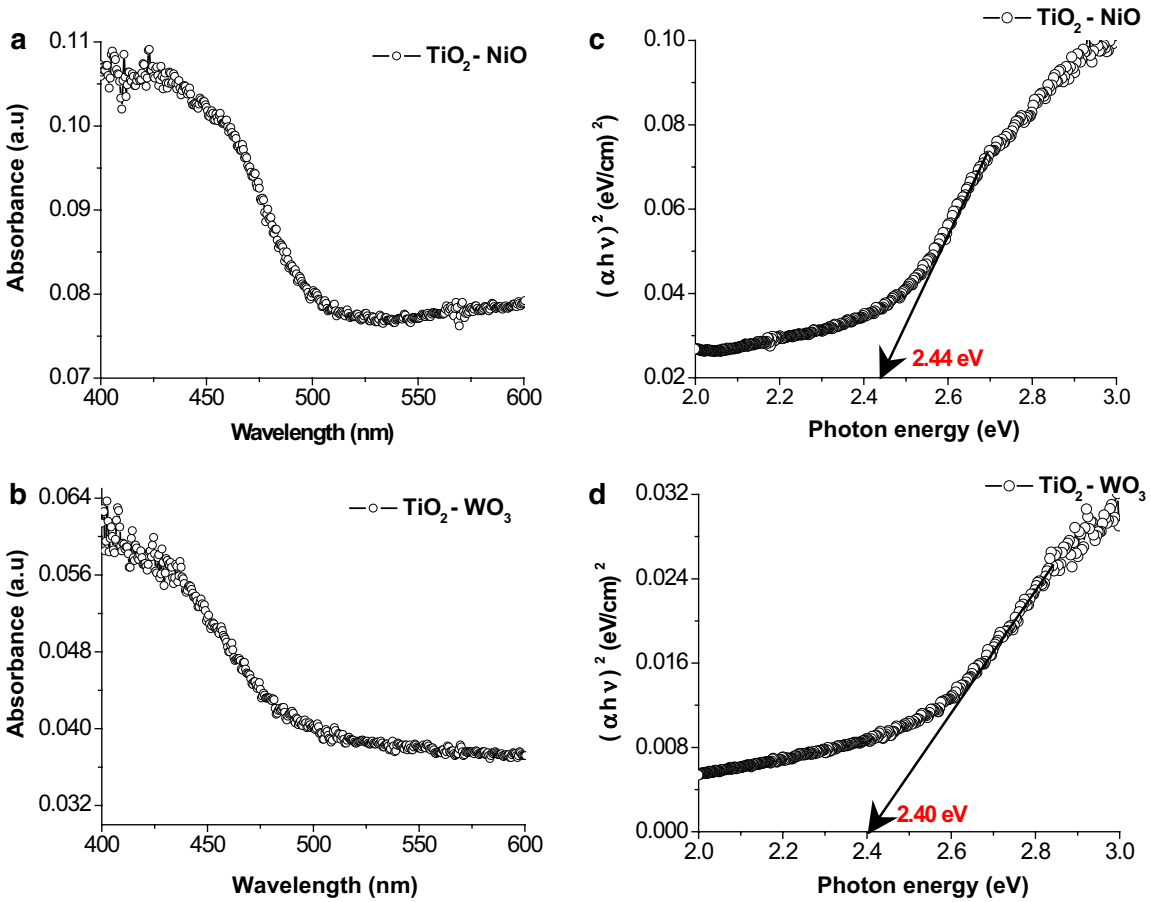

Fig. 7 DRS UV-Vis-IR spectra of **a** TiO_2–NiO nanocomposites and **b** TiO_2–WO_3 nanocomposite. **c** Tauc plot extrapolation of TiO_2–NiO nanocomposite. **d** Tauc plot extrapolation of TiO_2–WO_3 nanocomposite

Figure 8b shows the photocatalytic activity of TiO_2–NiO nanocomposite. It could be seen that the inclusion of NiO nanoparticles on the matrix of anatase-rutile mixed TiO_2 exhibits a significant influence on the photocatalytic activity. In the presence of a small amount of NiO nanoparticles was obviously enhanced the photocatalytic acitivity as compared to pure anatase-rutile TiO_2 nanoparticles. Figure 8b illustrate the TiO_2–NiO nanocomposite photocatalytic mechanism. Under the direct solar irradiation, the photogenerated electrons on the conduction band of TiO_2 can transfer to NiO. The recombination of photogenerated electrons and holes are retarded by inclusion of NiO nanoparticles on anatase-rutile mixed TiO_2 matrix. Moreover the reason for this efficient achievement was tentatively credited to the inhibition of recombination of electron–hole pairs on the surface of the TiO_2. This is due to the (O^{2-}) oxygen vacancy site in anatase-rutile TiO_2, which coupled with NiO, to produce a close contact TiO_2–NiO nanocomposite particle providing a successful lane for electrons to move from one grain to another.

Figure 8d illustrate the photocatalytic activity mechanism of TiO_2–WO_3 nanocomposite. Better photocatalytic efficiency was achieved for TiO_2–WO_3 nanocomposite. The increased efficiency of this materials could be attributed to the light absorption of TiO_2–WO_3 shifted towards the visible region. An efficient charge separation could be assured because the photogenerated electrons from TiO_2 are transferred into the lower energy conduction band of WO_3. The generated holes in the valence band of WO_3 are moved into the higher energy valence band of TiO_2, which makes charge separation more efficient. In this way, life time of photogenerated electron–hole pairs is increased. In addition, to it can suppressed the photogenerated electrons from recombination, thus increasing the charge transfer efficiency. The result was that the TiO_2–WO_3 nanocomposite photocatalyst exhibited even higher photocataltic activity than that of TiO_2–NiO nanocomposites.

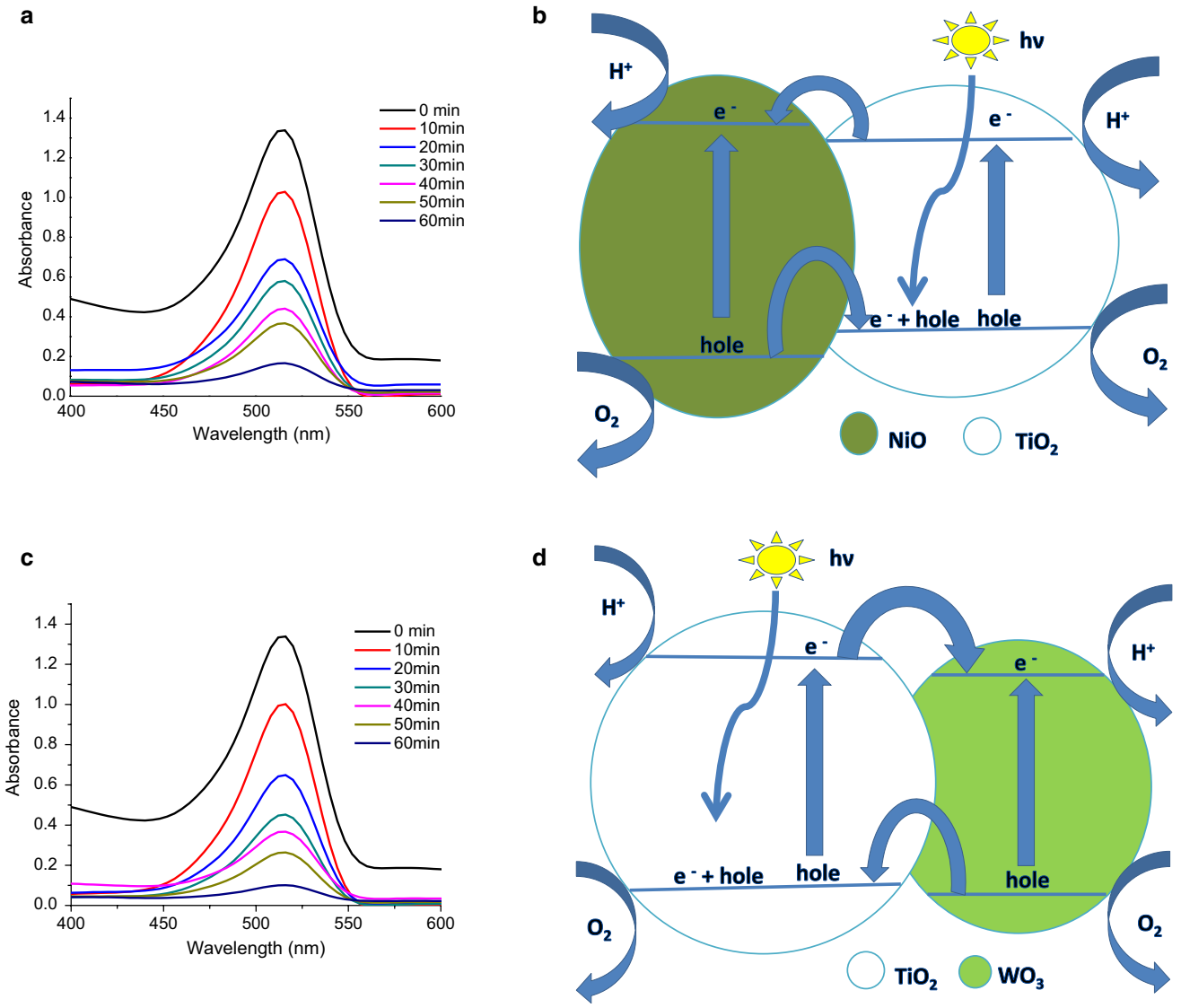

Fig. 8 **a** UV absorption spectra of eosin-Y solution treated with TiO_2–NiO nanocomposites. **b** Photocatalytic mechanism of TiO_2–NiO nanocomposite. **c** UV absorption spectra of eosin-Y solution treated with TiO_2–WO_3 nanocomposites. **d** Photocatalytic mechanism of TiO_2–WO_3 nanocomposite

Table 5 Zeta potential, electrophoretic mobility and optical band gap of nanocomposite

Nanocomposite	Zeta potential (mV)	Electrophoretic mobility $\times 10^{-6}$(cm^2/Vs)	Optical band gap (eV)
TiO_2–NiO	1.1	9	2.44
TiO_2–WO_3	−1.5	−12	2.40

Even though more number of Bragg's diffraction planes were informed that the TiO_2–WO_3 nanocomposite have better electrons transport track as compared to the TiO_2–NiO nanocomposite as shown in Figs. 1, 2. The bigger and uniform particle size distribution of TiO_2–WO_3 nanocomposites was clear evidence for the better photocatalytic activity. In addition, Table 5 shows the 550 °C annealed TiO_2–WO_3 nanocomposite in a suspension had large zeta values, which repelled each other and did not have a tendency flocculate. The higher zeta value indicated the greater stability of TiO_2–WO_3 nanocomposite in aqeuos solution. TiO_2–WO_3 nanocomposites had better zeta potential, electrophoretic mobility and optical band gap as compared to the TiO_2–NiO nanocomposites.

4 Conclusion

TiO_2–NiO and TiO_2–WO_3 nanocomposites were prepared by hydrothermal and surface modification methods and analyzed using X-ray diffraction, SEM, TEM, EDAX, Zeta potential, electrophoretic mobility and Photocatalytic activity measurements. The nanocomposite structural features were investigated using the Rietveld refinement method Jana 2006. The cell parameters, phase fraction, crystallite size, particle size, atomic position and bond length between atoms in each phase is affected by the addition of NiO and WO_3 to the mixed anatase-rutile TiO_2. The photocatalyst performance was found to increased by the usage of TiO_2–WO_3 nanocomposites as compared to TiO_2–NiO nanocomposite, which was due to the light absorption shifted towards the visible region, reduced the photogenerated electron–hole recombination and the life time of photogenerated electron–hole pairs increased. In addition, the larger and uniform particle size distribution of TiO_2–WO_3 nanocomposites created better photocatalytic efficiency.

References

1. S.M. Hosseinpour-Mashkani, M. Maddahfar, A. Sobhani-Nasab, Precipitation synthesis, characterization, morphological control and photocatalyst application of $ZnWO_4$ nanoparticles. J. Electron. Mater. **45**(7), 3612–3620 (2016)
2. S.M. Hosseinpour-Mashkani, M. Ramezani, A. Sobhani-Nasab, M. Esmaeil-Zare, Synthesis, characterization and morphological control of $CaCu_3Ti_4O_{12}$ through modified sol-gel method. J. Mater. Sci. **26**, 6086–6091 (2015)
3. S.M. Hosseinpour-Mashkani, M. Maddahfar, A. Sobhani-Nasab, Novel silver-doped CdMoO4: synthesis, characterization and its photocatalytic performance for methyl orange degredation through the sonochemical method. J. Mater. Sci. **27**, 474–480 (2016)
4. S. Choi, M.-S. Lee, D.-W. Park, Photocatalytic performance of TiO_2/V_2O_5 nanocomposite powder prepared by DC arc plasma. Curr. Appl Phys. **14**, 433–438 (2014)
5. K. Balachandran, R. Venckatesh, R. Sivaraj, P. Rajiv, TiO_2 nanoparticles versus TiO_2–SiO_2 nanocomposites: a comparative study of photo catalysis on acid red 88. Spectrochim. Acta Part A Mol. Biomol. Spectrosc. **128**, 468–474 (2014)
6. J. Wang, Z. Jiang, L. Zhang, P. Kang, Y. Xie, Y. Lv, Xu Rui, X. Zhang, Sonocatalytic degradation of some dyestuffs and comparison of catalytic activities of nano-sized TiO_2, nano-sized ZnO and composite TiO_2/ZnO powders under ultrasonic irradiation. Ultrason. Sonochem. **16**, 225–231 (2009)
7. Z. Liu, K. Pan, M. Wang, M. liu, Q. Lü, Y. Bai, T. Li, Influence of the mixed ratio on the photocurrent of the TiO_2/SnO_2 composite photoelectrodes sensitized by mercurochrome. J. Photochem. Photobiol. A **157**, 39–46 (2003)
8. R. Subasri, T. Shinohara, Investigations on SnO_2–TiO_2 composite photoelectrodes for corrosion protection. Electrochem. Commun. **5**, 897–902 (2003)
9. G. Zhang, H. Huang, L. Wenfang, Y. Fei, W. Huijun, L. Zhou, Enhanced photocatalytic activity of CoO/TiO_2 nanotube composite". Electrochim. Acta **81**, 117–122 (2012)
10. H. Qin, W. Congcong, L. Cao, B. Chi, J. Pu, L. Jian, A novel TiO_2 nanowires/nanoparticles composite photoanode with SrO shell coating for high performance dye-sensitized solar cell. J. Power Sources **226**, 8–15 (2013)
11. X. Qi, G. Su, G. Bo, L. Cao, W. Liu, Synthesis of NiO and NiO/TiO_2 films with electrochromic and photocatalytic activities. Surf. Coat. Technol. **272**, 79–85 (2015)
12. M. Liang, M. Liu, T. Peng, K. Fan, L. Lu, K. Dai, Fabrication and properties of meso-macroporous electrodes screen-printed from mesoporous titania nanoparticles for dye-sensitized solar cells. Mater. Chem. Phys. **118**, 477–483 (2009)
13. G.-S. Guo, H. Chao-Nan, Z.-H. Wang, F.-B. Gu, D.-M. Han, Synthesis of titania and titanate nanomaterials and their application in environmental analytical chemistry". Talanta **72**, 1687–1692 (2007)
14. Y. Liu, C.-Y. Liu, Q.-H. Rong, Z. Zhang, Characteristics of the silver-doped TiO_2 nanoparticles. Appl. Surf. Sci. **220**, 7–11 (2003)
15. B. Jiang, H. Yin, T. Jiang, J. Yan, Z. Fan, L. Changsheng, W. Jing, Y. Wada, Size-controlled synthesis of anatase TiO_2 nanoparticles by carboxylic acid group-containing organics. Mater. Chem. Phys. **92**, 595–599 (2005)
16. S. Nakade, S. Kambe, M. Matsuda, Y. Saito, T. Kitamura, Y. Wada, S. Yanagida, Electron transport in electrodes consisting of metal oxide nano-particles filled with electrolyte solution. Physica E **14**, 210–214 (2002)
17. B. Tan, B. Gao, J. Guo, X. Guo, M. Long, A comparison of TiO_2 coated self-cleaning cotton by the sols from peptizing and hydrothermal routes. Surf. Coat. Technol. **232**, 26–32 (2013)
18. Y.-F. Li, W.-P. Zhang, X. Li, Y. Yu, TiO_2 nanoparticles with high ability for selective adsorption and photodegradation of textile dyes under visible light by feasible preparation. J. Phys. Chem. Solids **75**, 86–93 (2014)
19. J. Fana, L. Zhenzhen, W. Zhou, Y. Miao, Y. Zhang, J. Hu, G. Shao, Dye-sensitized solar cells based on TiO_2 nanoparticles/nanobelts double-layered film with improved photovoltaic performance. Appl. Surf. Sci. **319**, 75–82 (2014)
20. A. Chowdhury, A. Kudo, T. Fujita, M.-W. Chen, T. Adschiri, Nano-twinned structure and photocatalytic properties under visible light for undoped nano-titania synthesised by hydrothermal reaction in water–ethanol mixture. J. Supercrit. Fluids **58**, 136–141 (2011)
21. D. Zhang, T. Yoshida, K. Furuta, H. Minoura, Hydrothermal preparation of porous nano-crystalline TiO_2 electrodes for flexible solar cells. J. Photochem. Photobiol. A **164**, 159–166 (2004)
22. W. Sigmund, H. EI-Shall, D.O. Shah, B.M. Moudgil, *Particulate Systems in Nano and Biotechnologie*. (CRC press, Taylor and Francis Group, Boca Raton, 2009)
23. P. Mohanty, S. Saravanakumar, R. Saravanan, C. Rath, TiO_2 nanowires grown from nanoparticles: structure and charge density study. J. Nanosci. Nanotechnol. **13**, 1–7 (2013)
24. V. Petricek, M. Dusek, L. Palatinus, *The Crystallographic Computing System*. (Institute of Physics, Prague, 2006)
25. S. Saravanakumar, R. Saravanan, S. Sasikumar, Effect of sintering temperature on magnetic properties and charge density distribution of nano-NiO. Chem. Paper (2013). doi:10.2478/s11696-013-0519-1
26. P.M. Woodward, A.W. Sleight, T. Vogt, Structure refinement of triclinic tungsten trioxide. J. Phys. Chem. Solids **56**(10), 1305–1315 (1995)
27. E. Indrea, E. Bica, E.-J. Popovici, R.-C. Suciu, M.C. Rosu, T.-D. Silipas, Rietveld refinement of powder X-ray diffraction

of nanocrystalline noble metals-tungsten trioxide. Rev. Roum. Chim. **56**(6), 589–593 (2011)
28. Y. Ku, C.-N. Lin, W.-M. Hou, Characterization of coupled NiO/TiO_2 photocatalyst for the photocatalytic reduction of Cr(VI) in aqueous solution. J. Mol. Catal. A **349**, 20–27 (2011)
29. K. Momma, F. Izumi, VESTA 3 for three-dimensional visualization of crystal, volumetric and morphology data. J. Appl. Crystallogr. **44**, 1272–1276 (2011)
30. D.T. Cromer, R. Herrington, The structure of anatase and rutile. J. Am. Chem. Soc. **77**(18), 4708–4709 (1954)
31. L. Vegard, Result of crystal analysis. Phil. Mag. **32**(187), 65–96 (1916)
32. P. Scherrer, Bestimmung der Grösse und der inneren Struktur von Kolloidteilchen mittels Röntgenstrahlen. Nachrichten von der Gesellschaft der Wissenschanften zu Göttingen **26**, 98–100 (1918)
33. J.I. Langford, A.J.C. Wilson, Scherrer after sixty years: a survey and some new results in the determination of crystallite size. J. Appl. Crystallogr. **11**, 102–113 (1978)